

FREE NEUTRON EJECTION FROM SHOCK BREAKOUT IN BINARY NEUTRON STAR MERGERS

AYAKO ISHII,¹ TOSHIKAZU SHIGEYAMA,¹ AND MASAOMI TANAKA^{2,3}

¹*Research Center for the Early Universe, Graduate School of Science, University of Tokyo, Bunkyo-ku, Tokyo 113-0033, Japan*

²*Astronomical Institute, Tohoku University, Aoba, Sendai 980-8578, Japan*

³*National Astronomical Observatory of Japan, Osawa, Mitaka, Tokyo 181-8588, Japan*

(Received xxx; Revised xxx; Accepted xxx)

Submitted to ApJ

ABSTRACT

Merging neutron stars generate shock waves that disintegrate heavy nuclei into nucleons especially in the outer envelope. It is expected that some of these neutrons having avoided capturing positrons, remain as free neutrons even after the disappearance of electron–positron pairs. To investigate how many free neutrons can be ejected from merging neutron stars, we performed special-relativistic Lagrangian hydrodynamics computations with simplified models of this phenomenon in which a spherically symmetric shock wave propagates in the hydrostatic envelope and emerges from the surface. We systematically study a wide parameter space of the size of the merging neutron stars and the energy involved in the shock waves. As a result, it is found that the mass of remaining free neutrons is 10^{-7} to $10^{-6} M_{\odot}$, which is smaller than the previously expected mass by more than two orders of magnitude. There is a preferred energy of the order of 10^{48} erg that yields the maximum amount of free neutrons for large sizes of the envelope. We briefly discuss the emission from the free neutron layer and estimate the luminosity in the optical band to be about 7×10^{41} erg s⁻¹ ($M_n/10^{-6} M_{\odot}$) in ~ 30 minutes after the merger.

Keywords: gravitational waves — hydrodynamics — nuclear reactions, nucleosynthesis, abundances
— relativistic process — shock waves — stars: neutron

arXiv:1805.04909v2 [astro-ph.HE] 18 Jun 2018

1. INTRODUCTION

Gravitational waves (GW170817) from a binary neutron star merger (NSM) were detected by LIGO on 2017 August 17 UT (Abbott et al. 2017a). The electromagnetic wave counterpart was also detected over the wide wavelength range (Fermi-LAT Collaboration 2017; Goldstein et al. 2017; Abbott et al. 2017c; Savchenko 2017; Evans et al. 2017; Haggard et al. 2017; Abbott et al. 2017b; Shappee et al. 2017; Troja et al. 2017; Kilpatrick et al. 2017; Kasliwal et al. 2017; Drout et al. 2017; Nicholl et al. 2017; Soares-Santos et al. 2017; Lipunov et al. 2017; Hu et al. 2017; Arcavi et al. 2017a,b; Díaz et al. 2017; Andreoni et al. 2017; McCully et al. 2017; Valenti et al. 2017; Pian et al. 2012; Smartt et al. 2017; Hallinan et al. 2017; Alexander et al. 2017; Kim et al. 2017; Tominaga et al. 2017). The optical counterpart (SSS17a) was discovered by the Swope Supernova Survey 10.9 hr after GW170817 (Coulter et al. 2017). This observation singled out the host galaxy as an S0 galaxy NGC 4993. The distance to this galaxy was estimated to be ~ 40 Mpc.

The following optical and near-infrared observations (e.g. Cowperthwaite et al. 2017; Chornock et al. 2017; Utsumi et al. 2017; Coulter et al. 2017; Tanvir et al. 2017) have revealed that the emission in optical bands decays in a couple of days, while the emission in near-infrared bands lasted for about 10 days. The optical counterpart is thought to originate from matter ejected from the NSM and is referred to as a kilonova or macronova (Li & Paczyński 1998; Kulkarni 2005; Metzger et al. 2010). The ejecta are composed of nascent r-process elements, most of which are radioactive and thus work as a heat source. Theoretical models of kilonovae (Kasen et al. 2013; Barnes & Kasen 2013; Tanaka & Hotokezaka 2013; Tanaka et al. 2017a,b; Kasen et al. 2017) have shown that the ejecta that include a significant amount of lanthanide elements are much more opaque for optical photons than the ejecta composed of Fe. As a consequence, it is predicted that a kilonova is brighter in near the infrared bands than in the optical, and can keep its brightness for about 10 days, depending on the ejecta mass. The features of the near infrared emission of SSS17a, which are consistent with predictions, enable estimations of the ejecta mass ($\sim 0.03 M_{\odot}$) and the mean velocity ($\sim 0.1c$, where c denotes the speed of light; Tanaka et al. (2017b)).

The follow-up observations started in 10.9 hr after the merger event. If the earlier emission from the NSM had been detected, it would have provided us with a different kind of information (Arcavi 2018). For example, it was suggested by smoothed particle hydrodynamics (SPH) simulations that the outermost layers in the ejecta are composed of free neutrons with a mass of the order of $10^{-4} M_{\odot}$ (Bauswein et al. 2013; Just et al. 2015; Goriely et al. 2015). The layer expands at a speed higher than $0.1c$. If this is true, the free neutron layer might contribute the earlier emission because free neutrons decay on a time scale of ~ 10 minutes (Metzger et al. 2015). Another interesting possibility is that the emission from the cocoon may be produced by a jet crossing the ejecta (Gottlieb et al. 2018; Kasliwal et al. 2017).

The emission powered by decays of free neutrons is not fully understood. The existence of the free neutron layer was explored using a small number of SPH particles in their simulations (Metzger et al. 2015). We need to confirm if this is the case or we need to know under what conditions the free neutron layer can be ejected. NSMs have also been investigated using grid-based simulations. For example, Sekiguchi et al. (2011) and Paschalidis et al. (2012) systematically studied NSMs by performing grid-based simulations and showed that shock waves broke out of matter near the contact surface of the two neutron stars (see Figure 1) though their simulations could not resolve matter with a mass down to $10^{-4} M_{\odot}$. Kyutoku et al. (2014) discussed the omnidirectional emission from this kind of shock breakout.

In this paper, we anticipate that the shock heating might disintegrate matter into free neutrons and protons and that the resultant layer containing free neutrons contributes to the early emission. To investigate this possibility, we utilize simplified spherically symmetric models in which we calculate the propagation of a shock wave generated deep inside the surface layer with a density distribution following a power-law function of the distance to the surface.

The paper is organized as follows. In Section 2, we describe the setup of our simplified models in detail and introduce the numerical scheme we use to calculate the shock propagation and the subsequent phenomena. In Section 3, we present our results. Finally, in Section 4 we summarize the conditions for realizing a free neutron layer and discuss emission from this layer.

2. METHODS

In a real NSM event, matter is ejected aspherically, so simulations for this event have been performed with numerical hydrodynamics codes fully incorporating multidimensionality. On the other hand, these comprehensive numerical studies may not be able to resolve the detailed structures close to the surface, which can affect emission in the early

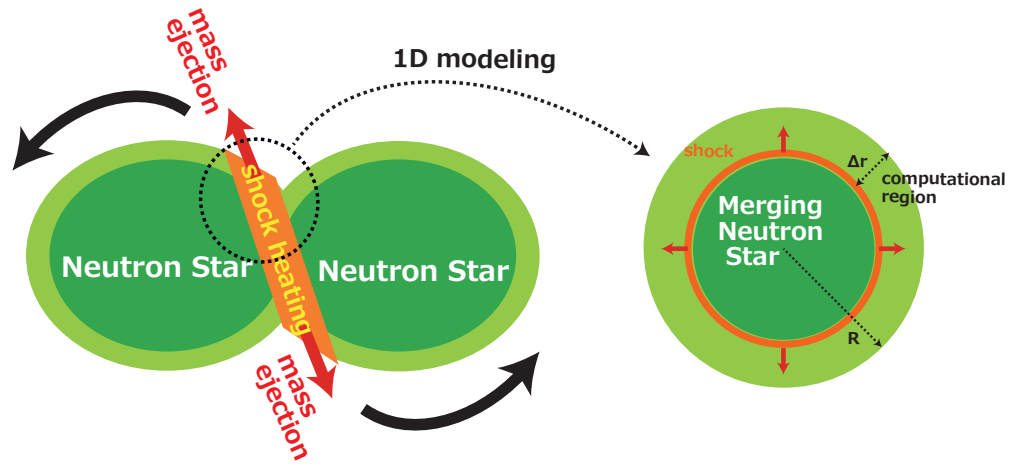


Figure 1. Schematic picture of the binary NSM in reference to [Kyutoku et al. \(2014\)](#). Shock waves are generated in coalescing double-neutron stars and propagate into the tidally disrupted matter. Some amount of material is ejected due to the shock heating. The thickness Δr of the outermost layer corresponds to the computational region and R is the radius of the surface.

phase of the event. The free neutron layer mentioned above is one example. Here, we employ an alternative approach by simplifying the situation as depicted in Figure 1, which is the strategy taken by [Kyutoku et al. \(2014\)](#).

2.1. Initial setting of our model

A spherical envelope in hydrostatic equilibrium is placed close to the surface with a mass density distribution $\rho(r) \propto (R - r)^3$, where R and r are the radius of the surface and the radial coordinate, respectively. [Kyutoku et al. \(2014\)](#) used $R = 15$ km for their fiducial value from results of numerical simulations. It is expected and confirmed that a smaller radius requires a stronger shock to eject the same amount of the envelope, thus leading to a higher density of positrons, and reducing the mass of free neutrons by the positron capture process. Therefore, we explore models with $R = 15 - 30$ km to search for optimal conditions for free neutrons. The thickness Δr of the outermost layer (corresponding to the computational region) is determined so that the total mass M_{env} involved in this region becomes $10^{-3} M_{\odot}$. The resultant Δr takes the value of a few $\times 10^{-2} R$ with $R = 15 - 30$ km. This value of M_{env} is chosen to be significantly greater than the mass of ejecta to reduce the influence of the method of the initial energy input to generate a shock wave on the amount of free neutrons. The gravitational energies of the envelope, less than -10^{50} erg, guarantee that only a part of the envelope finally becomes unbound.

The pressure $P(r)$ in this region is assumed to be dominated by degenerate ultra-relativistic electron gas given by

$$P(r) = \frac{(3\pi^2)^{1/3} \hbar c}{4} \left(\frac{Y_e \rho(r)}{m_u} \right)^{4/3} \equiv K \rho(r)^{4/3}, \quad (1)$$

where \hbar , Y_e , and m_u denote the Dirac constant, the electron fraction per nucleon, and the atomic mass unit, respectively. Here, we assume that Y_e has a constant value of 0.1 to mimic the beta equilibrium in cold dense matter. A shock wave is generated by increasing the thermal energy in the innermost region.

2.2. Hydrodynamics code

To describe the shock propagation in the envelope, we have developed a special-relativistic Lagrangian hydrodynamics code based on the previous work introduced in [Wilson & Mathews \(2003\)](#). Equations of Lagrangian hydrodynamics with the time t and radial coordinates r are written as follows:

$$\frac{dD}{dt} + D \frac{\partial r^2 v_r}{r^2 \partial r} = 0, \quad (2)$$

$$\frac{dE}{dt} + E \frac{\partial r^2 v_r}{r^2 \partial r} + P \left[\frac{d\Gamma}{dt} + \Gamma \frac{\partial r^2 v_r}{r^2 \partial r} \right] = 0, \quad (3)$$

$$\frac{dS_r}{dt} + S_r \frac{\partial r^2 v_r}{r^2 \partial r} + \frac{\partial P}{\partial r} + \frac{GM\rho}{r^2} = 0, \quad (4)$$

where v_r , Γ , G , and M are the radial velocity, the Lorentz factor, the gravitational constant, and the mass of a merging object, respectively. The term $GM\rho/r^2$, expressing the gravitational force per volume, is added to the momentum equation. We have fixed the value of M to $2 M_\odot$ throughout the computations. Here, we have chosen a mass significantly smaller than the total mass of the merging object ($\sim 2.8M_\odot$) to partially take into account the effects of the centrifugal force on the surface gravity in our spherically symmetric model. The Lorentz-contracted state variables D , E , and S_r denote the coordinate baryon mass density, the coordinate internal energy density, and the coordinate momentum density, respectively, and can be expressed with the mass density ρ , the specific internal energy ϵ defined in the comoving frame, and v_r as

$$D = \Gamma\rho, \quad (5)$$

$$E = \Gamma\rho\epsilon, \quad (6)$$

$$S_r = (D + \gamma E)\Gamma v_r. \quad (7)$$

We use the ultra-relativistic equation of state $P = \rho\epsilon/3$ and thus $\gamma = 4/3$. The finite difference approach was adopted with a leapfrog scheme and the artificial viscosity method was employed. The computation was performed in the geometrical units with $G = c = 1$.

This Lagrangian hydrodynamics code was validated through solutions of some shock tube problems presented in [Martí & Müller \(2003\)](#) and we have confirmed that the code reproduces the results of a known self-similar solution ([Sakurai 1960](#)) relevant to our present work, in which a shock wave propagates in a non-uniform medium through the medium-vacuum interface.

We use 500 computational cells to cover the entire region. We initiate calculations by increasing the thermal energy in the innermost 10 cells to generate a strong shock wave. We use the final kinetic energy E_f to distinguish models with different inputs of the thermal energy inputs. The velocity at the innermost computational cell is always set to be zero to mimic the stiff outer crusts of the neutron stars.

The temperature T after the passage of the shock is derived from the formula

$$P = \frac{a_r T^4}{3} + K\rho^{4/3}, \quad (8)$$

where a_r is the radiation constant ($= 7.56 \times 10^{-15} \text{ erg cm}^{-3} \text{ K}^{-4}$). Here, the pressure is approximated by the sum of the radiation pressure and the degeneracy pressure of ultra-relativistic electron gas.

2.3. Abundance of free neutrons

We have calculated the temporal evolution of the mass fraction of free neutrons in each cell after the shock hits the cell. It is assumed that the shock wave immediately disintegrates nuclei of heavy elements to free nucleons due to high temperatures ($T > 10^{10} \text{ K}$) at the shock front. Then, the positron capture process, $n + e^+ \rightarrow p + \bar{\nu}_e$, decreases the number of these free neutrons, while the electron capture process, $p + e^- \rightarrow n + \nu_e$, produces free neutrons. Since the timescale of the positron capture process τ_+ is given in [Metzger et al. \(2015\)](#) as

$$\tau_+ \simeq 2.1 \left(\frac{kT}{\text{MeV}} \right)^{-5} \text{ s} \quad (9)$$

while the timescale of the electron capture process τ_- is given in [Kawano \(1992\)](#), we calculate the temporal variation of the mass fraction of free neutrons X_n by integrating

$$\frac{dX_n}{dt} = -\frac{X_n}{\Gamma\tau_+(T)} + \frac{(1 - X_n)}{\Gamma\tau_-(T)}, \quad (10)$$

with respect to the time t in the rest-frame of each cell to estimate how many free neutrons can be ejected, because the outermost layer expands with highly relativistic speeds. The initial value of X_n is set to be 0.9 according to the beta equilibrium of cold dense matter (see section 2.1).

After the temperature in each cell decreases down to 10^{10} K , we perform nuclear reaction network calculations using a code developed by one of the authors ([Shigeyama et al. 2010](#)), with the initial conditions (i.e., the abundances of protons

Table 1. Ejecta masses and ejected free neutron masses for 16 different models.

| R | E_f | M_{ej} | M_n |
|------|-----------|----------------------|----------------------|
| (km) | (erg) | (M_\odot) | (M_\odot) |
| 15 | 10^{47} | 6.4×10^{-7} | 3.8×10^{-7} |
| 15 | 10^{48} | 6.0×10^{-6} | 9.2×10^{-7} |
| 15 | 10^{49} | 4.7×10^{-5} | 7.6×10^{-7} |
| 15 | 10^{50} | 3.0×10^{-4} | 1.5×10^{-6} |
| 20 | 10^{47} | 8.6×10^{-7} | 5.4×10^{-7} |
| 20 | 10^{48} | 7.9×10^{-6} | 2.1×10^{-6} |
| 20 | 10^{49} | 6.1×10^{-5} | 1.5×10^{-6} |
| 20 | 10^{50} | 3.9×10^{-4} | 2.0×10^{-6} |
| 25 | 10^{47} | 1.1×10^{-6} | 7.0×10^{-7} |
| 25 | 10^{48} | 1.0×10^{-5} | 3.6×10^{-6} |
| 25 | 10^{49} | 7.4×10^{-5} | 2.8×10^{-6} |
| 25 | 10^{50} | 4.6×10^{-4} | 2.6×10^{-6} |
| 30 | 10^{47} | 1.3×10^{-6} | 8.5×10^{-7} |
| 30 | 10^{48} | 1.2×10^{-5} | 5.2×10^{-6} |
| 30 | 10^{49} | 8.9×10^{-5} | 4.7×10^{-6} |
| 30 | 10^{50} | 5.4×10^{-4} | 3.7×10^{-6} |

and neutrons) given by the above calculations to check how many free neutrons remaining at the temperature of 10^{10} K prevent from positron capture reactions and neutron capture reactions by heavier nuclides at lower temperatures.

Here, neutrino cooling of the ejecta is neglected. The timescale for the e^+e^- pair annihilation ($\sim 10^{-4}$ s) is longer than the expansion timescale even at the highest temperature of $\sim 10^{11}$ K in our computations (Chiu 1961).

3. RESULTS

3.1. Overview of shock breakouts

We have performed simulations for the 16 models listed in Table 1: We have calculated models with four different values for the radii $R = 15, 20, 25,$ and 30 km. For each value of R , models with four different values of the final kinetic energies E_f , i.e., $10^{47}, 10^{48}, 10^{49},$ and 10^{50} erg have been calculated.

First, we present the results of a model with $R = 25$ km and $E_f = 10^{49}$ erg. Figure 2 shows the temporal evolutions of the density ($\Gamma\rho$), the velocity (Γv_r), and the temperature. Here, the left column shows the profiles before the shock breakout and the right one shows those after the shock breakout. The outermost region is accelerated to relativistic speeds (the middle right panel) and is consistent with Kyutoku et al. (2014). The temperature at the shock front always exceeds 10^{11} K (the bottom left panel). Actually, most of the ejecta experience a maximum temperature above 10^{10} K (see the right panel of Figure 3). At these temperatures, the most stable nuclei ^{56}Fe are disintegrated to $13\alpha+4n$ and subsequently α nuclei are disintegrated to free nucleons on much shorter timescales than the light crossing time of the envelope, $\sim 10^{-4}$ s. Thus, whatever elements exist before the merger, all the elements in the envelope will be disintegrated into nucleons after the shock passage because even the most stable nucleus ^{56}Fe can be disintegrated by the shock. Then, a free neutron captures a positron on a time scale of $\sim 2.1 \times 10^{-5}$ s at $\sim 10^{11}$ K (cf., eq. (9)), which is comparable to the timescale of the adiabatic cooling and might be longer, especially in the outer region where the shock cannot heat up the matter to such high temperatures.

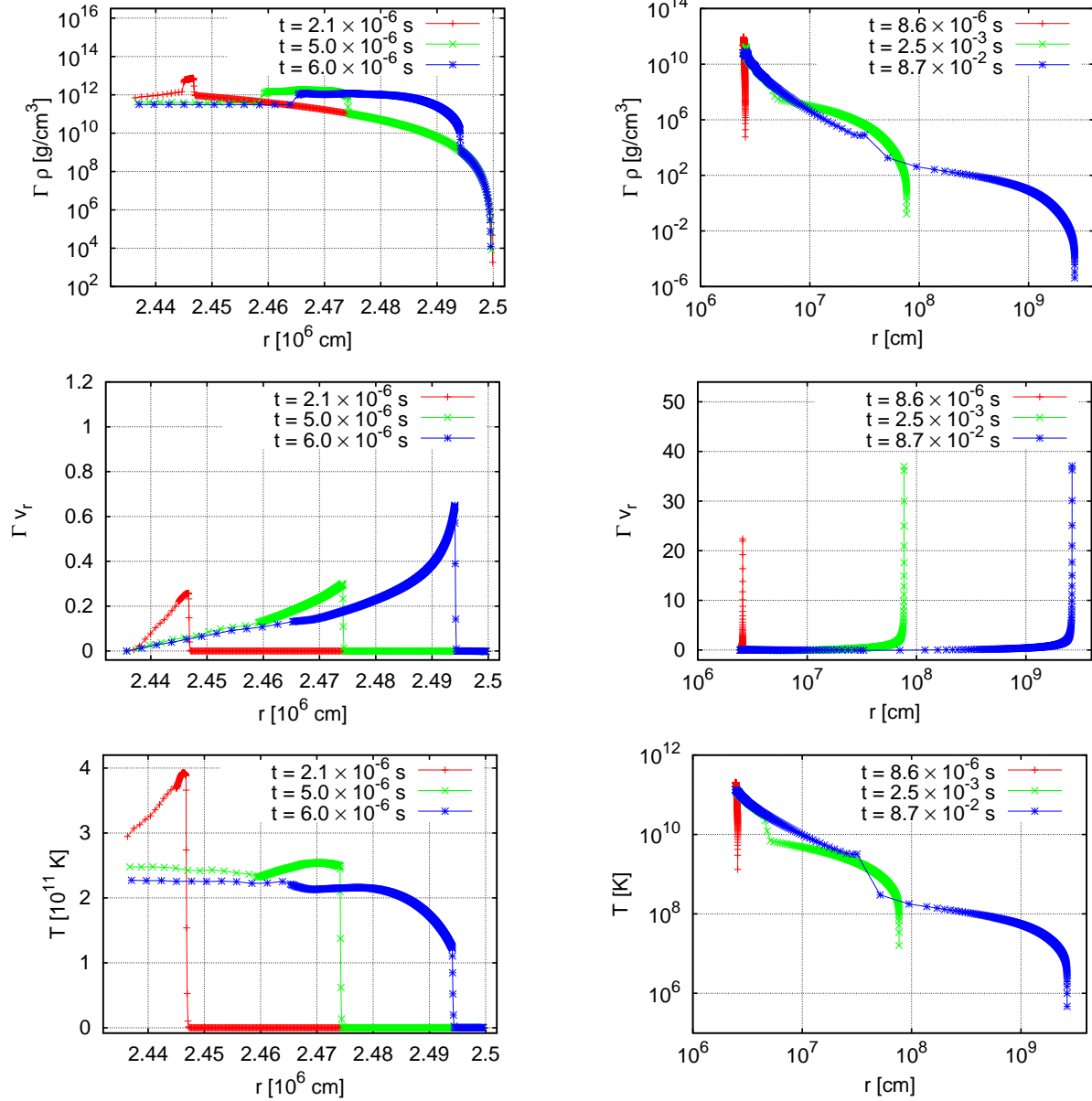


Figure 2. Temporal evolution of the density (top panels), the velocity (middle panels), and the temperature (bottom panels) profiles for a model with $R = 25$ km and $E_f = 10^{49}$ erg. The left column shows the profiles before the shock breakout and the right column shows those after the shock breakout.

3.2. Free neutron layers

Figure 3 shows a snapshot of the distribution of the mass density $\Gamma\rho$ at $t = 1.8 \times 10^{-2}$ s and a distribution of the maximum temperature of each fluid element with respect to the four-velocity Γv_r (in units of the speed of light) for models with $E_f = 10^{49}$ erg. Note that these figures show only the ejected part of the envelope.

Figure 4 shows the results of nucleosynthesis calculations when the temperature in all the cells becomes $< 10^8$ K. As the temperature decreases down below 10^{10} K, the reactions $p(n, \gamma)d$ occur and the resultant deuterons quickly fuse to produce ${}^4\text{He}$. In the inner region, one after another, the residual neutrons are captured by the nuclei and produce heavy neutron-rich elements ($\Gamma v_r < 0.6$ in Figure 4). In the outer layer ($\Gamma v_r > 0.6$), the lower density prohibits

neutron captures. Consequently, the nucleosynthesis no longer occurs and the outermost layers contain free neutrons and ${}^4\text{He}$. In other words, the r-process freezes out in the outer layer. Since the mass of the ejecta is concentrated in the inner region ($\Gamma v_r < 1$) as indicated by the left panel of Figure 3, the free neutron layer occupies only a fraction of the total ejecta mass. The ejecta masses M_{ej} and the ejected free neutron masses M_n in each model, with different R and E_f are plotted in Figure 5 and summarized in Table 1.

The ejecta mass increases with increasing radius R for the same E_f due to decreasing surface gravities. Though the ejecta mass also increases monotonically with increasing E_f , a higher E_f leading to higher temperatures behind the shock wave shortens the timescale of the positron capture process through eq. (9) and reduces X_n . In models with small R , positron captures monotonically decrease the fraction of free neutrons as a function of E_f , while the faster expansion resulting from a larger E_f inhibits neutron captures by heavy nuclei. These two factors determine the behavior of M_n as a function of E_f in the top panels of Figure 5. In models with larger radii, the lower expansion rates do not significantly inhibit neutron capture by heavy nuclei even with a high E_f . Thus, M_n does not increase in the models with $E_f = 10^{50}$ erg in the bottom panels of Figure 5. As a result, the maximum value of M_n over all of our models is $5.2 \times 10^{-6} M_\odot$, with $R = 30$ km and $E_f = 10^{48}$ erg.

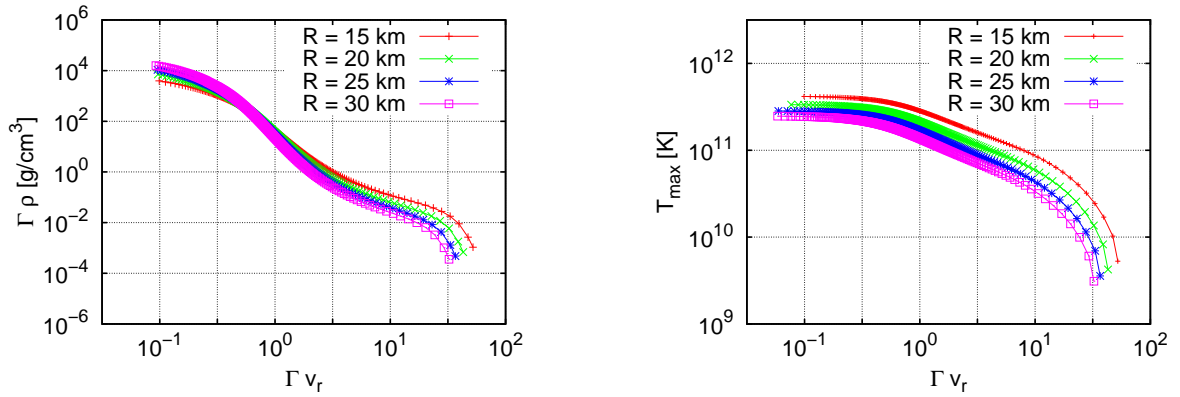


Figure 3. Snapshot of the distribution of the mass density at $t = 1.8 \times 10^{-2}$ s (left panel), and the distribution of the maximum temperature (right panel), with respect to the final velocity Γv_r , for models with $E_f = 10^{49}$ erg.

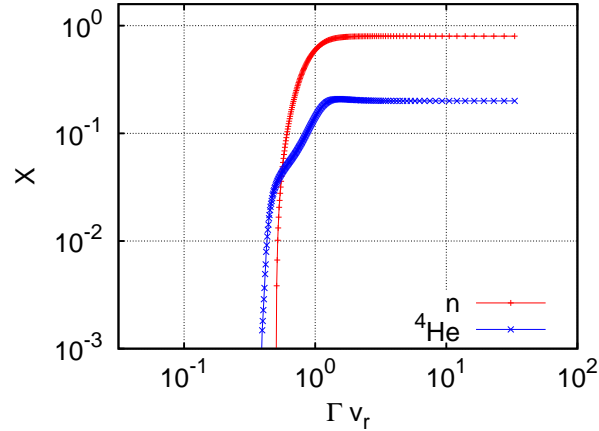


Figure 4. Distributions of the mass fraction of free neutrons and ${}^4\text{He}$, with respect to the final velocity Γv_r , for models with $R = 25$ km and $E_f = 10^{49}$ erg at $t = 9.3 \times 10^{-2}$ s, with a temperature $< 10^8$ K in all the cells.

The emission from the outer ejecta composed of free neutrons is discussed in the next section.

4. CONCLUSIONS AND DISCUSSION

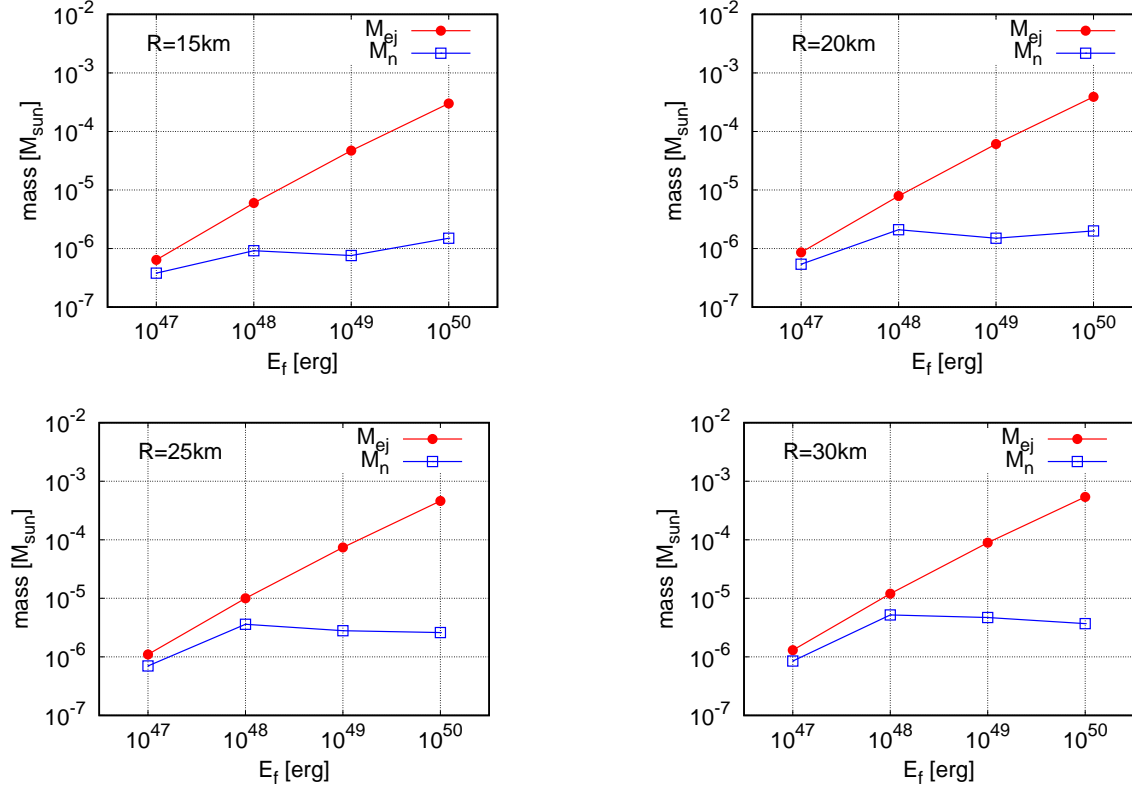


Figure 5. Mass M_{ej} of ejecta and the mass M_n of ejected free neutrons with respect to E_f . The top left panel shows models with $R = 15$ km, the top right panel shows those with $R = 20$ km, the bottom left panel shows those with $R = 25$ km, and the bottom right panel shows those with $R = 30$ km.

To examine the possibility of ejecting free neutrons from the envelope of binary NSMs as previously claimed by [Just et al. \(2015\)](#), we have constructed simplified models in which spherically symmetric envelopes in hydrostatic equilibrium are expelled by strong shocks initiated by sudden injection of thermal energies. To investigate what conditions maximize the yields of free neutrons, we have calculated 16 models by changing R and E_f . The mass of the envelope is set to be $10^{-3} M_{\odot}$ for all the models. Our results suggest that the ejecta mass is no more than a half of this initial envelope mass, even for an extremely large E_f of 10^{50} erg and R of 30 km (see Table 1).

Our series of simulations suggest that it is likely that an energy level of 10^{48} erg is preferable for free neutron ejection for the models with larger R . If the energy is smaller than this threshold, then the shock cannot eject enough amount of the envelope. If the energy is larger, too high temperatures behind the shock front convert free neutrons to protons by positron captures. The mass M_n of ejected free neutrons is maximized with $E_f = 10^{48}$ erg and is of the order of $10^{-6} M_{\odot}$, even for a model with an extremely large $R = 30$ km. We have obtained the values of M_n that are more than two orders of magnitude smaller than those in [Just et al. \(2015\)](#). The distribution of X_n is qualitatively consistent with the previous works, though the total amount of free neutrons is still significantly smaller. This indicates that free neutrons in the previous works originated from a different mechanism, such as the tidal debris and/or the neutrino-driven wind, while only the shock-heated ejecta are considered in this work.

The initial mass fraction X_n is determined by assuming that the nuclei of heavy elements are disintegrated to free neutrons and protons because of shock heating, which is an endothermic reaction. The effects of the energy being consumed by the endothermic reaction are not considered in our models. The energy density is calculated by $a_r T^4 / \rho \sim 3 \times 10^{19}$ erg g^{-1} at the shock front, with $T \sim 2.5 \times 10^{11}$. Since the energy of the endothermic reaction for Fe is ~ 9 MeV per nucleon, the energy density for the reaction is calculated by $9 \text{ MeV} / m_n \sim 8.6 \times 10^{18}$ erg g^{-1} . Thus, the energy is brought out by the endothermic reaction by a few tens of a percent. The shock speed and temperature

at the shock front are decrease due to the reaction, and the positron capture process becomes unfavorable, resulting in a large amount of X_n . Here, the largest amount of expelled energy by the endothermic reaction is considered for the most stable element, Fe; thus the expelled energy might decrease for realistic compositions of the merging neutron stars.

Metzger et al. (2015) discussed the emission from ejecta composed of some free neutrons. They assumed that the opacity of the ejecta is due to lanthanide elements. Our models suggest that the ejecta eventually becomes composed of hydrogen, helium, and neutron-rich heavy elements after beta decays. In addition, the amount of free neutrons is much smaller than that in the previous studies. Nevertheless, depending on the viewing angle, one can observe emission from the ejecta in this study. Thus, the situation may change as follows. Suppose that the mass M_{ej} and energy of the ejecta are $10^{-5} M_\odot$ and 10^{48} erg, then the mean velocity of the ejecta becomes $\sim c/3$. The ejecta remains optically thick for $\sqrt{\kappa M_{ej}/4\pi}/(c/3) \sim 2.5 \times 10^3$ s as long as the matter is still fully ionized and the opacity is dominated by Thomson scattering, i.e., $\kappa \sim 0.4 \text{ cm}^2 \text{ g}^{-1}$. Due to the small opacities, the characteristic timescale of the emission becomes shorter than previously expected. The time it takes for the diffusion velocity of photons to become comparable to the expansion velocity ($c/3$) is about $t_{ch} \sim 1500$ s.

The typical temperature and luminosity of the emission at this characteristic timescale can be estimated as follows. The beta decay of a neutron supplies an energy of 300 keV on a timescale of ~ 800 s. Thus, the energy density at this time is given by $\epsilon_0 \sim 300 \text{ keV} \times (M_n/m_n)/[4\pi \times (800 \text{ s} \times c/3)^3/3] \sim 10^6 \text{ erg cm}^{-3} (M_n/3.6 \times 10^{-6} M_\odot)$, which corresponds to a temperature of $\sim 10^5$ K, assuming radiation-dominated ejecta. Subsequent adiabatic expansion lowers this temperature and a typical temperature at $t_{ch} \sim 1500$ s is $\sim 5.3 \times 10^4$ K. The luminosity L is estimated as

$$L \sim 4\pi(ct/3)^2 v_{diff} \epsilon_0 (800 \text{ s}/t)^4 \sim 7.6 \times 10^{41} \text{ erg s}^{-1} \left(\frac{t}{1500 \text{ s}} \right)^{-2} \left(\frac{M_n}{3.6 \times 10^{-6} M_\odot} \right), \quad (11)$$

where v_{diff} is the diffusion velocity when photons can diffuse out from the ejecta, which is $\sim c/9$.

According to the luminosity and temperature estimated above, the emission powered by decays of free neutrons mainly goes to ultraviolet wavelengths on a timescale of about 30 minutes. Assuming blackbody radiation, absolute magnitudes at 2000 and 2600 Å (UVW2 and UVW1 of *Swift*/UVOT) are about -13.55 and -13.25 mag, respectively (AB magnitude). These magnitudes correspond to the observed magnitudes of 19.45 and 19.75 mag at 40 Mpc, which are detectable with the *Swift* satellite if observations start immediately after the merger.

The presence of hydrogen in the outermost layers may also suggest an emission similar to that of Type II-P supernovae. Recombinations start in the outer layers and the ejecta are expected to emit the blackbody radiation with a temperature of ~ 6000 K, which corresponds to the recombination temperature of hydrogen in Type II-P supernovae (Shigeyama & Nomoto 1990; Popov 1993; Kasen & Woosley 2009). From these values, the luminosity in this recombination phase can be roughly estimated as $6 \times 10^{38} \text{ erg s}^{-1} (t/2.5 \times 10^3 \text{ s})^2 (T/6000 \text{ K})^4$ at the final stage of the photospheric emission.

If the emission from such ejecta can be detected, some information on the dynamics of the merging event can be extracted because the spectrum must involve individual line features associated with transitions of hydrogen and helium. This is in contrast to dynamical ejecta composed of lanthanide elements that create too many inseparable lines in the spectrum and hide the information on dynamics.

We are grateful to the anonymous referee for providing helpful comments on this manuscript. This work was supported by JSPS KAKENHI grants No. 16H06341, 16K05287, 15H02082, 15H02075, 16H02183, 17H06357, and 17H06363.

APPENDIX

A. TEST FOR GRID CONVERGENCE

We have performed calculations for a model with $R = 25$ km and $E_f = 10^{49}$ erg using 500 and 1000 computational cells. The calculation is initiated by increasing the thermal energy in the innermost 20 cells in the case with 1000 cells to generate a strong shock, which has the same volume as the innermost 10 cells in the case with 500 cells. Figure 6 shows a comparison of the profiles of the X_n distributions resulting from calculations using 500 and 1000 computational cells. Though the distribution in the case with 1000 cells extends to a larger Γv_r region than that with 500 cells, the masses of ejecta and free neutrons are $7.4 \times 10^{-5} M_\odot$ and $2.8 \times 10^{-6} M_\odot$ for the model using 500 cells

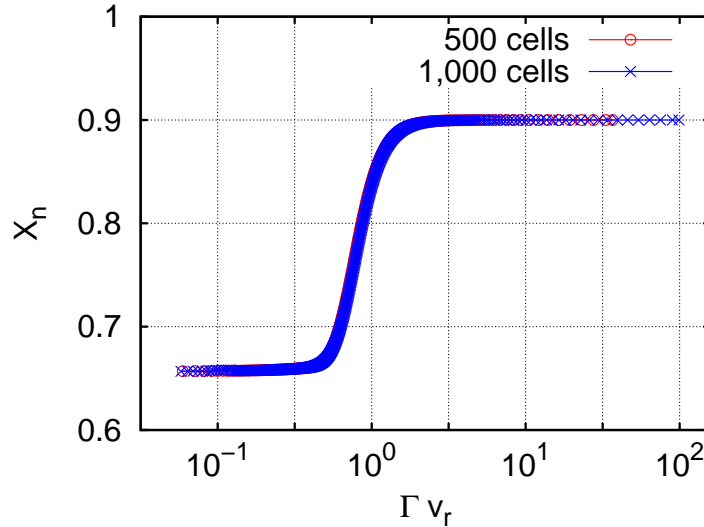


Figure 6. Comparison of distributions of X_n at the time $t = 5 \times 10^{-3}$ s between computations with 500 and 1000 computational cells.

and $7.7 \times 10^{-5} M_\odot$ and $2.7 \times 10^{-6} M_\odot$ for the model with 1000 cells. Therefore, the computations with 500 cells have already achieved enough convergence for our present purposes.

REFERENCES

- Abbott, B. P., Abbott, R., Abbott, T. D., et al. 2017, *Physical Review Letters*, 119, 161101
- Abbott, B. P., Abbott, R., Abbott, T. D., et al. 2017, *ApJL*, 848, L12
- Abbott, B. P., Abbott, R., Abbott, T. D., et al. 2017, *ApJL*, 848, L13
- Alexander, K. D., Berger, E., Fong, W., et al. 2017, *ApJL*, 848, L21
- Arcavi, I., McCully, C., Hosseinzadeh, G., et al. 2017, *ApJL*, 848, L33
- Arcavi, I., Hosseinzadeh, G., Howell, D., et al. 2017, *Nature*, 551, 64
- Arcavi, I. 2018, arXiv:1802.02164
- Andreoni, I., Ackley, K., Cooke, J., et al. 2017, *PASA*, 34, e069
- Barnes, J., & Kasen, D. 2013, *ApJ*, 775, 18
- Bauswein, A., Goriely, S., & Janka, H.-T. 2013, *ApJ*, 773, 78
- Chornock, R., Berger, E., Kasen, D., et al. 2017, *ApJL*, 848, L19
- Chiu, H. Y. 1961, *Annals of Physics*, 16, 321
- Coulter, D. A., Foley, R. J., Kilpatrick, C. D., et al. 2017, *Science*, 358, 1556
- Cowperthwaite, P. S., Berger, E., Villar, V. A., et al. 2017, *ApJL*, 848, L17
- Díaz, M. C., Macri, L. M., Garcia Lambas, D., et al. 2017, *ApJL*, 848, L29
- Drout, M. R., Piro, A. L., Shappee, B. J., et al. 2017, *Science*, 358, 1570
- Evans, P. A., Cenko, S. B., Kennea, J. A., et al. 2017, *Science*, 358, 1565
- Fermi-LAT Collaboration 2017, arXiv:1710.05450
- Haggard, D., Nynka, M., Ruan, J. J., et al. 2017, *ApJL*, 848, L25
- Hallinan, G., Corsi, A., Mooley, K., et al. 2017, *Science*, 358, 1579
- Hu, L., Wu, X., Andreoni, I., et al. 2017, arXiv:1710.05462
- Goldstein, A., Veres, P., Burns, E., et al. 2017, *ApJL*, 848, L14
- Goriely, S., Bauswein, A., Just, O., Pllumbi, E., & Janka, H.-T. 2015, *MNRAS*, 452, 3894
- Gottlieb, O., Nkar, E., Piran, T. 2018, *MNRAS*, 473, 576
- Just, O., Bauswein, A., Pulpillo, R. A., Goriely, S., & Janka, H.-T. 2015, *MNRAS*, 448, 541
- Kasen, D., & Woosley, S. E. 2009, *ApJ*, 703, 2205
- Kasen, D., Badnell, N. R., & Barnes, J. 2013, *ApJ*, 774, 25
- Kasen, D., Metzger, B., Barnes, J., Quataert, E., & Ramirez-Ruiz, E. 2017, *Nature*, 551, 80
- Kasliwal, M. M., Nakar, E., Singer, L. P., et al. 2017, *Science*, 358, 1559

- Kawano, L. 1992, NASA STI/Recon Technical Report N, 92, 1.
- Kilpatrick, C. D., Foley, R. J., Kasen, D., et al. 2017, *Science*, 358, 1583
- Kim, S., Schulze, S., Resmi, L., et al. 2017, *ApJL*, 850, L21
- Kulkarni, S. R. 2005, arXiv:astro-ph/0510256
- Kyutoku, K., Ioka, K., & Shibata, M. 2014, *MNRAS*, 437, L6
- Li, L.-X., & Paczyński, B. 1998, *ApJL*, 507, L59
- Lipunov, V. M., Gorbovskoy, E., Kornilov, V. G., et al. 2017, *ApJL*, 850, L1
- Martí, J. M., & Müller, E. 2003, *Living Reviews in Relativity*, 6, 7
- McCully, C., Hiramatsu, D., Howell, D. A., et al. 2017, *ApJL*, 848, L32
- Metzger, B. D., Martínez-Pinedo, G., Darbha, S., et al. 2010, *MNRAS*, 406, 2650
- Metzger, B. D., Bauswein, A., Goriely, S., & Kasen, D. 2015, *MNRAS*, 446, 1115
- Nicholl, M., Berger, E., Kasen, D., et al. 2017, *ApJL*, 848, L18
- Paschalidis, V., Etienne, Z. B., & Shapiro, S. L. 2012, *PhRvD*, 86, 064032
- Pian, E., D’Avanzo, P., Benetti, S., et al. 2017, *Nature*, 551, 67
- Popov, D. V. 1993, *ApJ*, 414, 712
- Sakurai, A. 1960, *Commun. Pure Appl. Math*, 13, 310
- Savchenko, V., Ferrigno, C., Kuulkers, E., et al. 2017, *ApJL*, 848, L15
- Sekiguchi, Y., Kiuchi, K., Kyutoku, K., & Shibata, M. 2011, *Physical Review Letters*, 107, 051102
- Shappee, B., Simon, J. D., Drout, M. R., et al. 2017, *Science*, 358, 1574
- Shigeyama, T., & Nomoto, K. 1990, *ApJ*, 360, 242
- Shigeyama, T., Nakamura, K., Tsujimoto, T., & Moriya, T. 2010, *American Institute of Physics Conference Series*, 1279, 415
- Soares-Santos, M., Holz, D. E., Annis, J., et al. 2017, *ApJL*, 848, L16
- Smartt, S. J., Chen, T. W., Jerkstrand, A., et al. 2017, *Nature*, 551, 75
- Tanaka, M., & Hotokezaka, K. 2013, *ApJ*, 775, 113
- Tanaka, M., Kato, D., Gaigalas, G., et al. 2017, arXiv:1708.09101
- Tanaka, M., Utsumi, Y., Mazzali, P. A., et al. 2017, *PASJ*, 69, 102
- Tanvir, N. R., Levan, A. J., González-Fernández, C., et al. 2017, *ApJL*, 848, L27
- Tominaga, N., Tanaka, M., Morokuma, T., et al. 2017, arXiv:1710.05865
- Troja, E., Piro, L., van Eerten, H., et al. 2017, *Nature*, 551, 71
- Utsumi, Y., Tanaka, M., Tominaga, N., et al. 2017, *PASJ*, 69, 101
- Valenti, S., Sand, D. J., Yang, S., et al. 2017, *ApJL*, 848, L24
- Wilson, J. R., & Mathews, G. J. 2003, *Relativistic Numerical Hydrodynamics*, by James R. Wilson and Grant J. Mathews, pp. 232. ISBN 0521631556. Cambridge, UK: Cambridge University Press, December 2003., 232